ACS OMEGA

http://pubs.acs.org/journal/acsodf

Article

Selective Conversion of Syngas to Olefins via Novel Cu-Promoted Fe/RGO and Fe−Mn/RGO Fischer−Tropsch Catalysts: Fixed-Bed Reactor vs Slurry-Bed Reactor

Al-Hassan Nasser,* Haitham M. El-Bery,* Hamada ELnaggar, Islam K. Basha, and Ahmed Abd El-Moneim

Cite This: *ACS Omega* 2021, 6, 31099−31111

Read Online

ACCESS | Metrics & More | Article Recommendations

ABSTRACT: Fischer−Tropsch has become an indispensable choice in the gas-to-liquid conversion reactions to produce a wide range of petrochemicals using recently emerging biomass or other types of feedstock such as coal or natural gas. Herein we report the incorporation of novel Cu nanoparticles with two Fischer−Tropsch synthesis (FTS) catalytic systems, Fe/reduced graphene oxide (rGO) and Fe−Mn/rGO, to evaluate their FTS performance and olefin productivity in two types of reactors: slurry-bed reactor (SBR) and fixed-bed reactor (FBR). Four catalysts were compared and investigated, namely Fe, $FeCu_7$, $FeMn_{10}Cu_7$, and $FeMn_{16}$, which were highly dispersed over reduced graphene oxide nanosheets. The catalysts were first characterized by transmission electron microscopy (TEM), nitrogen physisorption, X-ray fluorescence (XRF), X-ray diffraction (XRD), and H-TPR techniques. In the SBR, Cu enhanced olefinity only when used alone in $FeCu_7$ without Mn promotion. When used with Mn, the olefin yield was not changed, but light olefins decreased slightly at the expense of heavier olefins. In the FBR system, Cu as a reduction promoter improved the catalyst activity. It increased the olefin yield mainly due to increased activity, even if the CO_2 decreased by the action of Cu promoters. The olefinity of the product was improved by Cu promotion but it did not exceed the landmark made by $FeMn_{16}$ at 320 °C. The paraffinity was also enhanced by Cu promotion especially in the presence of Mn, indicating a strong synergistic effect. Cu was found to be better than Mn in enhancing the paraffin yield, while Mn is a better olefin yield enhancer. Finally, Cu promotion was found to enhance the selectivity towards light olefins C2−4. This study gives a deep insight into the effect of different highly dispersed FTS catalyst systems on the olefin hydrocarbon productivity and selectivity in two major types of FTS reactors.

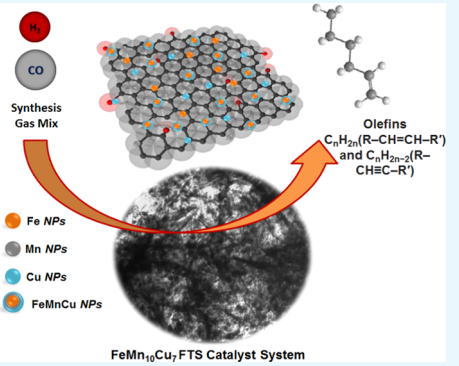

1. INTRODUCTION

Light olefins, especially ethylene, are economically valuable. They are utilized as vital building blocks to produce many essential end products in our daily lives (e.g., plastics, synthetic textiles, coatings, and solvents).[1,2] This crucial role of olefins rendered ethylene as the most produced hydrocarbon product worldwide.[3] As a result, enormous interest is oriented towards the production of olefins through a variety of petrochemical processes.[3−5] Most of these processes are petroleum-based, and with the rapid depletion of oil resources, the growing demand of light olefins has become a real challenge. Therefore, an alternative track for light olefin production that considers the environmental concerns has become indispensable. Fischer−Tropsch synthesis (FTS) is an intriguing route to non-petroleum countries to produce high added-value chemicals.[6−8] The major advantage of this process is the wide flexibility of the process in the aspects of syngas production and product distribution.[9] CO can be virtually produced from any incomplete combustion reaction of carbonaceous materials. These materials can range from coal and natural gas to biomass.[10] Hydrogen can be produced from the reforming of natural gas, electrolysis, and coal gasification, from catalytic gasification of biomass and fermentation[11,12] or water splitting.[13,14]

The products from the FTS process can be tailored according to the requirements of the local as well as international markets according to the targets defined for the process. Through decades of research, the modification of the system components can shift the selectivity and productivity of the process towards the desired hydrocarbon fractions. The variables that can be tuned are the catalyst composition, whether it is Fe- or Co-based, promoted or unpromoted, and supported or free-

Received: August 17, 2021
Accepted: October 28, 2021
Published: November 11, 2021

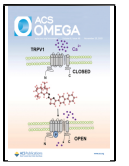

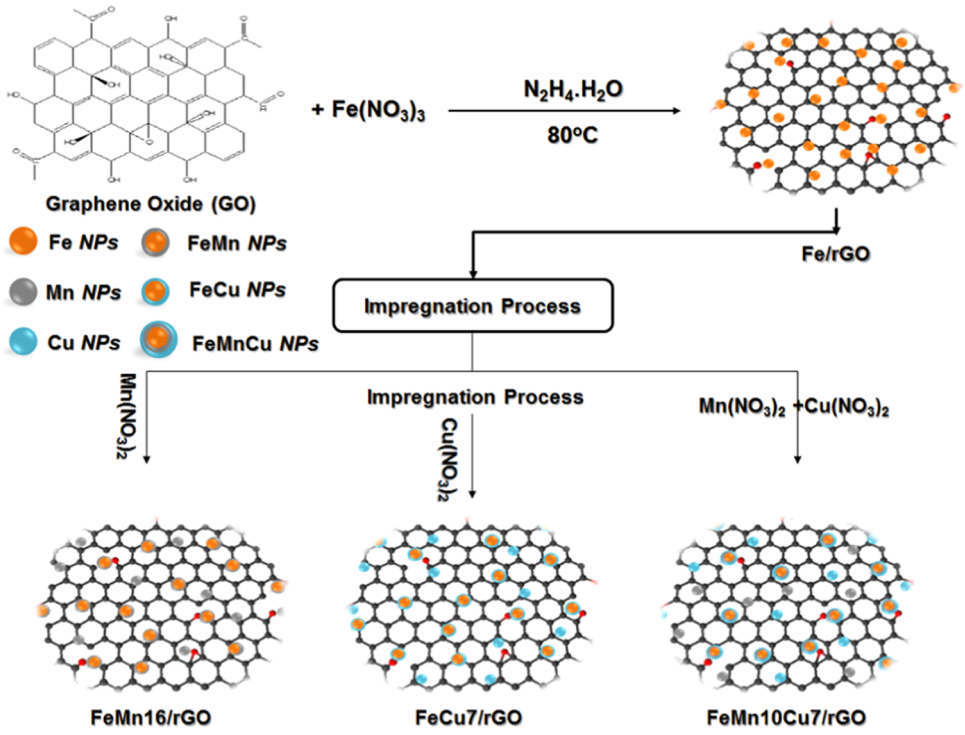

Figure 1. Synthesis scheme of FTS catalyst systems.

standing particles.[15,16] The type of support can also affect the catalyst performance through sintering inhibition and controlling the electron density on the main catalyst. Among those support materials, the ceramic supports (e.g., SiO_2, Al_2O_3, TiO_2) are the most widely studied and used.[8,17−22] Recently, carbon-based nanomaterials like carbon nanotubes,[23−25] graphene,[26−33] and other supports like metal-organic framework (MOF)[34] and porous organic polymer (POP)[35] are being investigated.

In addition to the abovementioned parameters, the reactor designs[4,36] as well as operating conditions play a crucial role in the product selectivity. The most common reactor designs used in research are the fixed-bed reactors (FBRs)[29,37] and the slurry-bed reactors (SBRs).[31,38,39] One of the most important operating conditions in FTS is the temperature. In general, the FTS processes are classified as either low-temperature Fischer−Tropsch (LTFT) or high-temperature Fischer−Tropsch (HTFT) systems.[40] The former is most commonly used with Co-based catalysts to produce straight long-chain products like diesel, lubricating oils, and waxes, while the latter is more commonly used with Fe-based catalysts since Co is known for its undesirable high methane selectivity in HTFT conditions.[41] On the other hand, Fe at high temperatures produces light olefins along with other lighter-end hydrocarbons at much higher selectivity.

It is generally accepted that Cu promotes Fe-based FTS catalysts by facilitating Fe-oxide reduction during the activation stage. Additionally, copper oxides are reduced easily to the zero-valent metallic state and at lower temperatures than Fe and Mn oxides.[42−45] The influence of Cu on the hydrocarbon distribution and especially olefin selectivity reported in the literature is rather cloudy. On the one hand, some works report that Cu has a negative effect on olefin selectivity since it gives rise to dissociative H_2 adsorption that encourages secondary olefin hydrogenation reactions,[43,46] while restricting dissociative CO desorption that is mainly responsible for chain growth, and prevents the hydrogenation of olefins. However, a contradicting view is also presented,[42,43] claiming that Cu increases surface alkalinity, which boosts the CO dissociative desorption, which in turn increases the surface concentration of the carbon radicals while depriving the surface from H_2 radicals. This in turn enhances chain growth and olefin selectivity. This effect was reported when Cu was used with other promoters due to the synergistic interaction between K and Cu as in an Fe−Cu−K unsupported catalyst[42] or in an Fe−Mn−K−Cu/SiO_2 catalyst.[43] However, the effect of Cu alone without K on the olefin selectivity was either not reported[42] or decreased the olefin selectivity.[43] Interestingly also, it was reported that Cu along with K can improve the olefin selectivity while lowering the chain growth probability.[47] Finally, O'Brien et al.[48] reported that Cu has no effect on product distribution and only enhanced the catalyst activity and olefin selectivity. This disagreement between different authors is due to the fact that FTS investigations are complicated and are often conducted at different conditions using a wide variety of catalysts.

Apart from detailed studies on the effects of the Cu promoter on the catalyst reduction and FTS properties, the synergistic effect of the Cu promoter alone or along with Mn supported on graphene nanosheets in both FBR and SBR has not been studied before. In addition, reduced graphene oxide (rGO) derived from cheap graphite powder is a potential competitor to conventional widely studied ceramic support materials from the point of cost and group of unique properties: for instance, high specific surface area, two-dimensional (2D) structure with well-developed porosity, and superior electronic, thermal, and mechanical properties.[49−51] It is noteworthy to mention that most of the previous studies that employed the Cu promoter have used ceramic-supported catalysts. Metal oxide supports are known for their strong metal−support interaction that hinders the active phase formation, and decreases the catalyst activity and FTS conversion with time.[52]

https://doi.org/10.1021/acsomega.1c04476
ACS Omega 2021, 6, 31099−31111

Therefore, in this work, for the first time up to our best knowledge, we report the preparation of Cu-promoted Fe and Fe−Mn/catalysts supported over graphene nanosheets to be characterized. Then the catalysts will be tested in both SBR and FBR Fischer−Tropsch systems to evaluate the effect of Cu on the overall performance and olefin productivity of the catalysts.

2. MATERIALS AND METHODS

2.1. Catalyst Preparations. Fe nanoparticles (NPs) were deposited on rGO sheets by the same method described in detail elsewhere,[31,53] as shown in Figure 1. To summarize, the Modified Hummer's method was used to produce graphite oxide (GtO) flakes using a mixture of H_2SO_4, HNO_3, and $KMnO_4$ (500, 160 mL, and 60 g, respectively) to oxidize graphite into graphite oxide (GtO). The produced mass was treated with H_2O_2 and then washed subsequently with HCl and distilled water (DW) followed by centrifugal separation to remove any remaining salts. The dried flakes were then dispersed ultrasonically in 200 mL DW, forming a suspension of graphene oxide (GO); this suspension was mixed with the doping solution containing an adequate amount of the Fe nitrate precursor salt dissolved in 50 mL of DW. The mixture was stirred mechanically for 8 h and then heated to 80 °C to be reduced by adding 22 mL of hydrazine hydrate (HH) 80% solution and then refluxed at 80 °C for 16 h. The produced powder after filtration was washed to neutral pH, dried, and stored in an airtight plastic box labeled Fe/rGO for later use.

Ultrasonic assisted impregnation was used for Cu and Mn promotion of the Fe/rGO catalysts.[53] The catalysts Fe/rGO (0.5 g) was ultrasonicated for 30 min in a ceramic crucible after being impregnated with 20 mL of ethanol solution of the nitrate precursors according to the required loading wt %. The slurry obtained after ultrasonication was steam dried over a beaker of boiling water while stirring continuously with a glass rod. Then the powder was dried at 60 °C for 3 h and stored in a glass vial. The vial was labeled $FeMn_xCu_y$, where x and y represent the moles of Mn and Cu/100 mol Fe, respectively, as determined by X-ray fluorescence (XRF) elemental analysis. If there was no Mn promoter in the catalyst, then the label used was $FeCu_y$ instead. The XRF analysis results of the produced catalysts are shown in Table 1.

Table 1. XRF Analysis Results for the Cu-Promoted Catalysts

	wt %					mol (100 mol Fe)	
catalyst	C	O	Fe	Cu	Mn	Cu	Mn
Fe	52.4	16.7	30.9				
$FeCu_7$	46.8	17.7	32.8	2.7		7.3	
$FeMn_{10}Cu_7$	49.4	20.4	25.7	2.1	2.4	7.0	9.7

2.2. Characterization. A Rigaku Ultima IV X-ray diffractometer was used to obtain the X-ray diffraction (XRD) patterns of the samples. The as-prepared and reduced (after TPR) catalysts were analyzed by exposing them to a Cu Kα source that radiates X-rays at λ = 0.154 nm, 40 kV, and 20 mA. The angle sweep range was 2θ = 5−80° at 0.02°/min. A transmission electron microscope (Hitachi H-7650 TEM) was used to study the morphology of the catalyst at 100 kV. N_2 adsorption isotherms of the degassed catalyst were produced using NOVA-2200e and Quantachrome Instruments equipment. These were used to calculate the Brunauer−Emmett−Teller (BET) surface area, total pore volume, and Barrett−Joyner−Halenda (BJH) pore radius. BELCAT-II, The Microtrac BEL instrument was utilized to study the reduction behavior of the catalysts under a stream of 5% vol H_2/Ar at 30 mL/min. The temperature program included heating to 300 °C at 10°/min, and then holding for 2 h under inert He atmosphere (30 mL/min). Afterwards, the temperature was decreased to 50 °C, then raised again to 800 °C at a rate of 5°/min, and then held constant at 800 °C for half an hour. The hydrogen consumption was monitored using an online TCD detector to detect the reduction peaks of the catalyst. Post-reduction XRD was carried out after the H-TPR by quickly transferring the catalyst to an airtight vessel and analyzing it in the XRD machine before severe oxidation took place. Finally, a Philips PW 2404 X-ray fluorescence instrument was used to obtain wave dispersive X-ray fluorescence (XRF) of the catalyst samples in order to find the bulk metal loading on the catalyst.

2.3. FTS Performance Evaluation. The slurry-bed reactor (SBR) shown in Figure 2 is the same unit used previously in the Fe−Mn investigation.[53] The other system used in this work was a fixed-bed reactor (FBR) that was slightly improved from the basic design described elsewhere,[29] as illustrated in Figure 3. The liquid traps in the old system that had a needlessly large volume were replaced by a 65 mL single cold trap operated at 3 °C so as to be similar to the one used in our previous publication.[53] Initially the catalyst (0.5 g) was diluted with an equal mass of SiC (0.5 g), mixed well using a mortar and pestle, then loaded in the reactor pipe (0.5 in ID). Reduction of the catalyst was carried out for 16 h at 450 °C under 50 mL/min flow of hydrogen gas. After the reduction was completed, the cold trap was prepared by adding 20 mL of distilled water and 2 g of n-octane, and the chiller was operated at 3 °C to cool down the cold trap. The desired reaction conditions were adjusted in the system including the CO/H_2 ratio of 1:1, temperature, pressure, and flow rate. During the run, the exit gas was analyzed using an online GC-TCD system equipped with a 3 m Shincarbon column (Restek) to measure the non-condensable gases (CO, CH_4, and CO_2). This system was calibrated using external gas standards. At the end of the run and after reaching the steady-state conditions, the hydrocarbons in the exit gas were measured by a GC-FID system fitted with a 30 m, 0.32 mm ID, and 10 μm film RT-Q PLOT capillary column (Restek). Methane standard was used as an external standard to calibrate the gas hydrocarbon concentrations. On the other hand, the liquid hydrocarbons condensed in the cold trap were analyzed by a Shimadzu-GCMS QP2010 system using a 60 m, 0.25 mm ID, and 0.25 μm film Agilent DB-5 column. In case of the liquid products, a 0.2 g n-dodecane internal standard was used for calibration and concentration calculations. The olefin concentrations in the gas and liquid products were monitored by producing an olefin-free sample by sulfuric acid absorption, and the difference in area was used to calculate the olefin concentrations. The equations used to calculate the conversion, selectivity, and yield of the reactor are shown below:

$$f_{CO}\% = \left(1 - \frac{F_{CO}}{y_{o\,CO} F_o}\right) \times 100$$

$$S\ \mathrm{Cmol}_{N,(o/p/i/t)}\% = \frac{\mathrm{FG}_{N,(o/p/i/t)} + \mathrm{FL}_{N,(o/p/i/t)}}{\sum_N F_{N,t}} \frac{\text{Cmol HC}}{\text{Cmol HC total}}$$

https://doi.org/10.1021/acsomega.1c04476
ACS Omega 2021, 6, 31099−31111

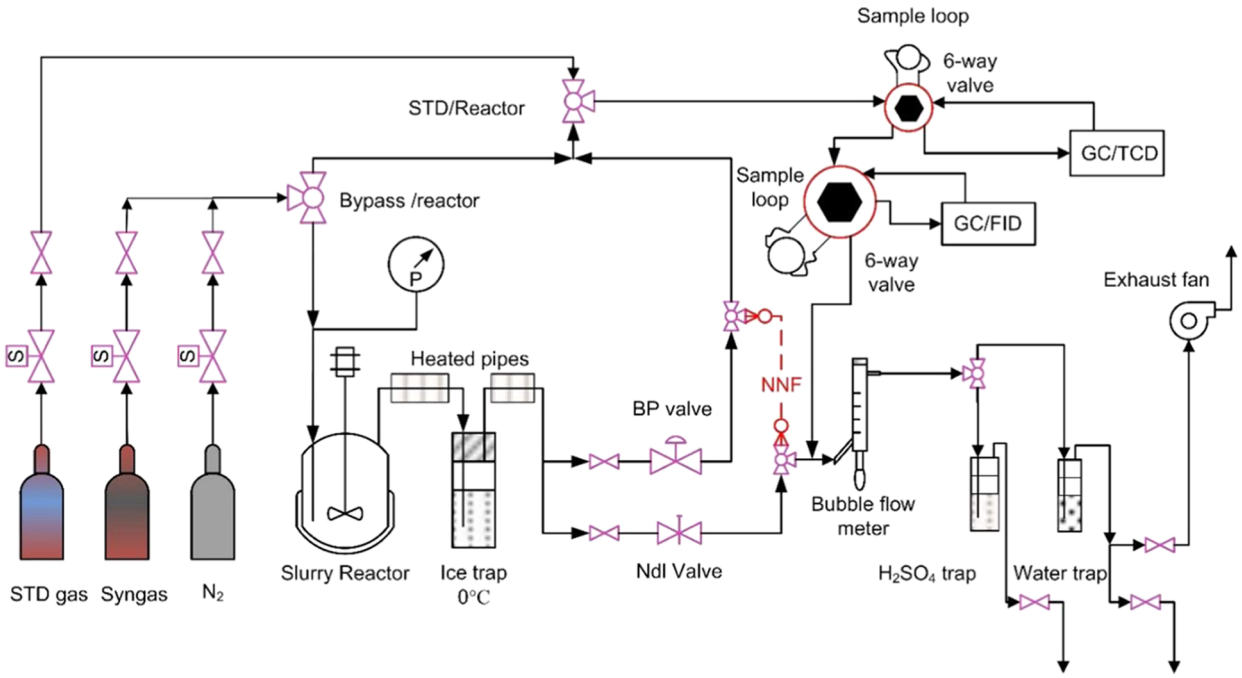

Figure 2. Process flow diagram of the slurry-bed reactor (SBR) unit (reprinted with permission from *RSC Adv*. 2018, 8 (27), 14854−14863).[53]

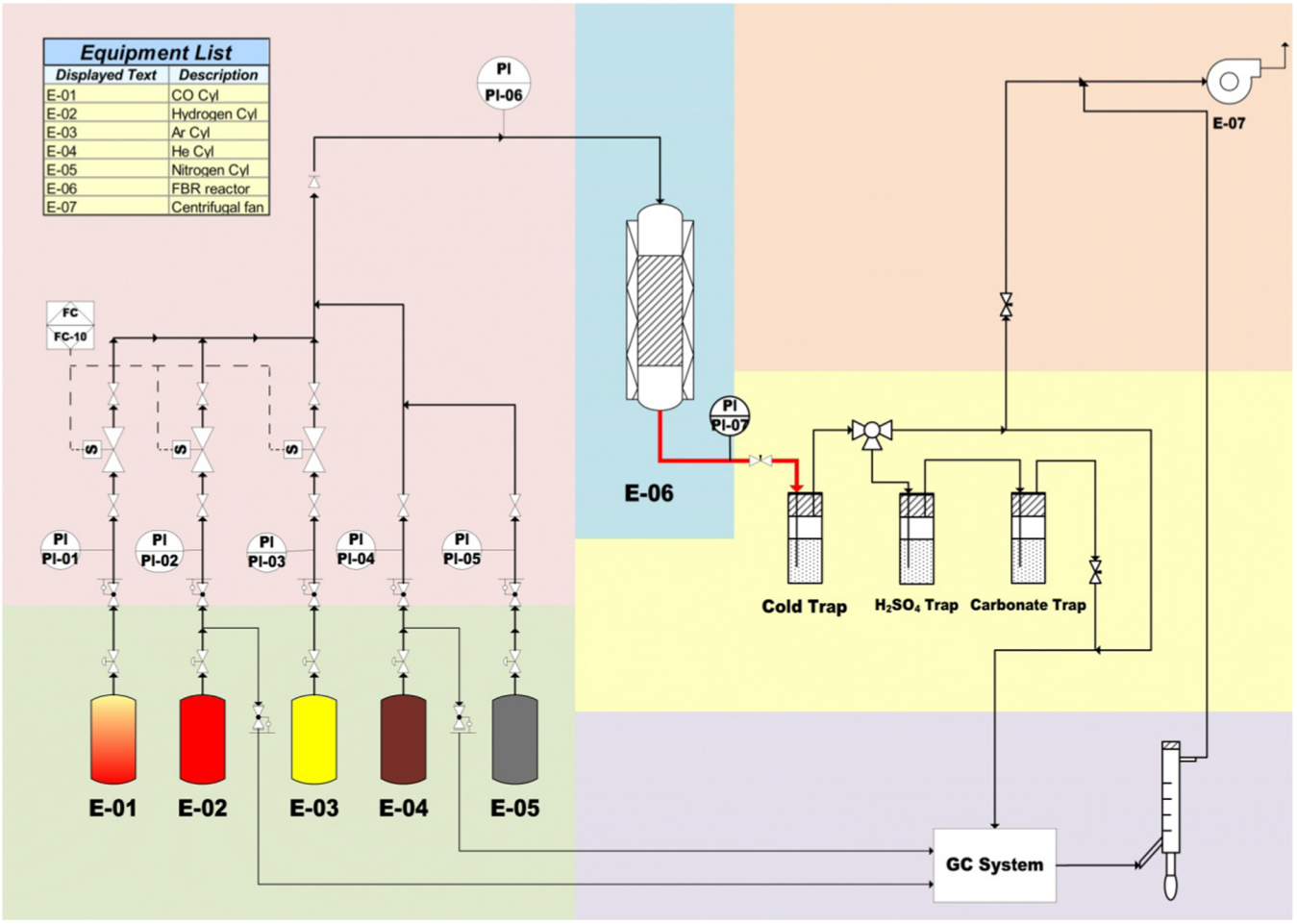

Figure 3. Process flow diagram of the modified FBR unit (reprinted with permission from *RSC Adv*. 2019, 9 (19), 10937−10937).[31]

https://doi.org/10.1021/acsomega.1c04476
ACS Omega 2021, 6, 31099−31111

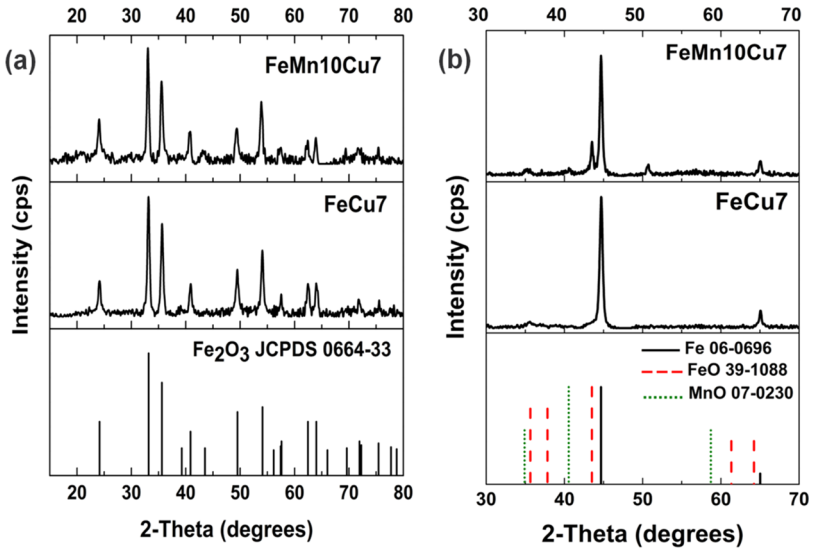

Figure 4. XRD results of the Cu-promoted catalysts: (a) as-prepared and (b) after TPR.

$$S\ \mathrm{mol}_{\mathrm{N},(o/p/i/t)}\% = \frac{\mathrm{FG}_{\mathrm{N},(o/p/i/t)} + \mathrm{FL}_{\mathrm{N},(o/p/i/t)}}{\sum_{\mathrm{N}} \mathrm{F}_{\mathrm{N,t}} \times \mathrm{N}_{\mathrm{N}}} \frac{\text{mol HC}}{\text{mol HC total}}$$

$$Y_{\mathrm{N}}\% = S\ C\mathrm{mol}_{\mathrm{N},(o/p/i/t)}\% \times (100 - S_{\mathrm{CO}_2}\%) \times f_{\mathrm{CO}}\% / 10000$$

where F is the molar rate, $f_{\mathrm{CO}}\%$ is the CO conversion, S is the selectivity, Y is the conversion, and y is the molar fraction, while FG and FL are the molar rates of the gas and liquid products, respectively.

3. RESULTS AND DISCUSSION

3.1. Structural and Morphological Properties (XRD and TEM). The XRD patterns for the as-prepared catalysts are demonstrated in Figure 4a. Similar to previous investigations of the Fe−Mn system, the hematite pattern is strongly recognized in the XRD spectra, proving once again that α-Fe_2O_3 is the main phase found in the catalyst after coprecipitation. The presence of Mn and Cu promoters did not produce any significant peaks due to their low crystallinity, low concentrations, high dispersion, or small grain sizes, rendering them undetectable by XRD. Metallic iron or α-Fe^0 is the major phase found after H_2 reduction of the catalysts, as can be clearly noticed from Figure 4b. FeO and MnO phases were present in $FeMn_{10}Cu_7$ as evidenced by their minor peaks, which shows that Mn has a retarding effect on the reduction of Fe-oxides.[53]

The XRD of the Mn-promoted spent iron catalyst was compared with the standard patterns of Fe_2C, Fe_5C_2 (Hagg carbide), and magnetite. The patterns clearly show the presence of the iron carbide phases in the spent catalyst, which shows that the active phase for the catalyst was the carbide form as discussed in our previous study.[53] FTS catalysts (Cu, Mn, and Mn−Cu) dispersed over reduced graphene oxide nanosheets were examined by TEM as presented in Figure 5. As shown, all metal catalysts' nanoparticles are highly dispersed over rGO nanosheets. The use of graphene oxide during the catalyst preparation scheme provides an excellent matrix for metal nanoparticle dispersion, as it is rich with oxygenated function groups that could act as perfect anchoring sites for FTS catalysts. Simultaneous reduction of GO and metal precursors results in the formation of structural defect sites, which are considered as catalytic active sites[52] and prevent metal nanoparticles from aggregation and sintering. This is unlike the traditional support materials that form strong metallic bonding with the metal FTS catalysts (iron silicate or iron aluminate) and cause a decrease in catalyst activity. It is also observed that the Cu-promoted FTS catalysts have a higher number of particles than the Cu-free catalyst.

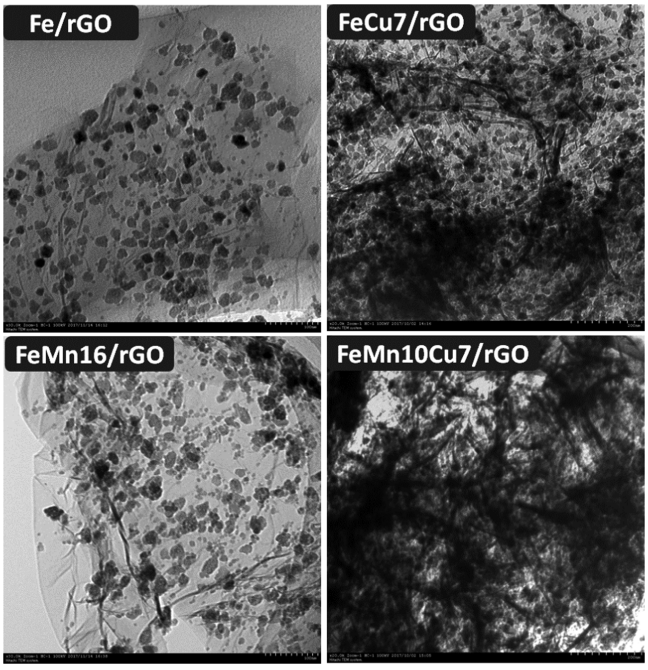

Figure 5. TEM images of FTS catalysts (Fe/rGO, $FeCu_7$, $FeMn_{16}$, and $FeMn_{10}Cu_7$/rGO).

3.2. H_2 Temperature-Programmed Reduction. The results obtained from the TPR tests are shown in Figure 6. An early peak (1) characteristic of Cu reduction is detected with the $FeCu_7$ sample at 240 °C.[42,43] However, it appears as a delayed peak (1′) at 330 °C when Mn is added in the $FeMn_{10}Cu_7$

https://doi.org/10.1021/acsomega.1c04476
ACS Omega 2021, 6, 31099−31111

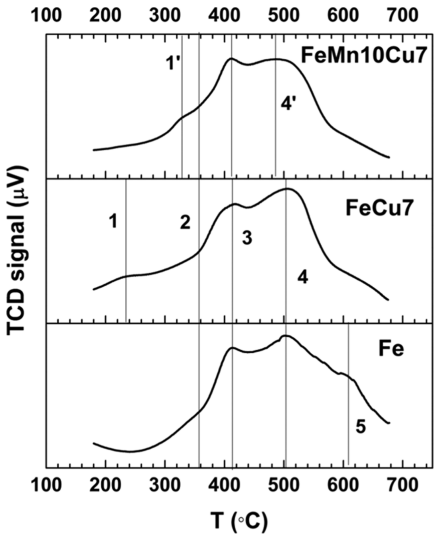

Figure 6. H_2-TPR results of the Cu-promoted catalysts compared with Fe.

sample. This further demonstrates that Mn can decrease the dissociative adsorption of H_2[23,41] and its retarding effect on all reactions requiring hydrogen radicals as a reactant, i.e., reduction and hydrogenation of olefins during the FTS reaction, which is supported by observations from the XRD pattern as previously discussed.

The effect of Cu as a reduction promoter, however, is also visible when Figure 6 is compared with the Mn H_2-TPR reported on our pervious study.[53] While all Cu-free Mn-promoted samples such as $FeMn_{16}$ and $FeMn_{29}$ still underwent reduction at temperatures beyond 600 °C, it can be clearly observed that all Cu-laden catalysts ended all reduction activity well before reaching 600 °C (at about 580 °C). Cu was reduced at early heating stages well before the reduction of Fe_2O_3; this provided valuable H_2 dissociation sites, which improved the reducibility of the catalyst and provided more active sites. This is expected to reflect on the FTS performance by enhancing the activity of the catalyst, recording higher conversions in the presence of Cu at the same operating conditions as compared with the Cu-free catalysts.[42,43]

The reduction of hematite (peak 3) occurred at about the same temperature of 420 °C with all catalysts; this happened at a slightly slower rate with $FeMn_{10}Cu_7$, as indicated by the slower rise in TCD signal with the temperature at 360 °C (line 2). Apparently, the second and the last stages of reduction (peaks 4 and 5 in Fe) merged into one peak (peaks 4 and 4′) in the presence of copper. However, peak 4′ was smaller in height and broader due to the presence of Mn, indicating a more difficult reduction reaction. This agrees with the XRD data, which showed remnants of FeO after reduction of $FeMn_{10}Cu_7$ due to the incomplete reduction of FeO into metallic Fe.

3.3. Surface Texture and Properties via N_2 Physisorption. Nitrogen physisorption data are summarized in Table 2. The results show that Cu causes an increase in BET area, which increased from 218 with Fe to 240.4 m^2/g with $FeCu_7$. Mn on the other hand, as observed previously, causes a decrease in BET area, which fell to 230.1 m^2/g with $FeMn_{10}Cu_7$. The same trend is observed in both pore volume and pore size. The increased surface area with Cu promotion indicates an increase in the number of active sites on the catalyst surface, which is in good agreement with the observations collected so far from XRD and TPR investigations.

Table 2. N_2 Physisorption Results for the Cu-Promoted Catalysts

catalyst	BET area (m^2/g)	pore volume (cm^3/g)	average pore size (Å)
rGO	395.3	0.4604	23.3
Fe	218.1	0.3505	19.2
$FeCu_7$	240.4	0.4187	19.2
$FeMn_{10}Cu_7$	230.1	0.4146	19.2

3.4. SBR FTS Performance Evaluation. The catalysts were tested at 340 °C, 2 MPa, and 4.2 L/(g h) in the SBR reactor, and the results are detailed in Table 3 for $FeCu_7$ and $FeMn_{10}Cu_7$ as compared with Fe and $FeMn_{16}$, which were evaluated in a previous work at the same conditions[53] as summarized in Figure 7a,b. The use of Cu as a promoter in SBR caused only a little change in the catalyst activity, and the CO_2 and CH_4 selectivity. The effect is so little to be mentioned, reaching a maximum conversion of 87% with $FeCu_7$ when Fe gave a minimum of 83%. However, Cu influenced the total olefin selectivity, significantly raising it from 14% with Fe to 25% with $FeCu_7$; this agrees with the findings of O'Brien et al.[48] On the other hand, when Cu is combined with Mn, a qualitative improvement is observed instead, with the olefin fraction becoming slightly richer in heavy olefins C_{5-8} with $FeMn_{10}Cu_7$ (12%) than with $FeMn_{16}$ (9%), while the total olefin selectivity stayed at 21% for them both, as displayed in Figure 7b. Mn is known for its effect that enhances carburization reactions and impedes H_2 dissociation,[23,41,53] and so the rise in heavy olefin selectivity can be explained in this light. The highest O/P ratio and olefin yield were achieved with $FeCu_7$ (0.334 and 14%), followed by $FeMn_{16}$ (0.271 and 12%) and then $FeMn_{10}Cu_7$ (0.268 and 11%), with Fe (0.169 and 7%) being the least oriented towards olefins.

Table 3. Cu Promotion Effect on SBR Performance[a]

	Fe	$FeCu_7$	$FeMn_{10}Cu7$	$FeMn_{16}$
CO conversion (%)	83	87	83	84
carbon balance (%)	98	97	97	97
fraction	selectivity C (mol %)			
CO_2	38	35	36	34
CH_4	22	20	20	24
C2−4 olefin	8	9	9	12
C5−8 olefin	6	16	12	9
total olefin	14	25	21	21
C9 + HC	22	7	12	5
total paraffin	70	65	67	72
total iso	16	10	12	7
total par + iso	86	75	79	79
O/P	0.17	0.33	0.27	0.27
olefin yield	7	14	11	12
A	0.57	0.63	0.63	0.55

[a]Reaction conditions: H_2/CO = 1, 2 MPa, 340 °C, 4.2 L/(g h).

3.5. FBR FTS Performance Evaluation. The FBR performance of the catalysts will be analyzed through the parameters of conversion, selectivities, yields, and the O/P ratio. The full performance data of the catalysts in the FBR at 300 and 320 °C are detailed in Tables 4 and 5, respectively. Figure 8a,b demonstrates the variation in CO conversion, and CO_2 and CH_4 selectivities at 300 and 320 °C. It can be clearly seen from Figure

https://doi.org/10.1021/acsomega.1c04476
ACS Omega 2021, 6, 31099−31111

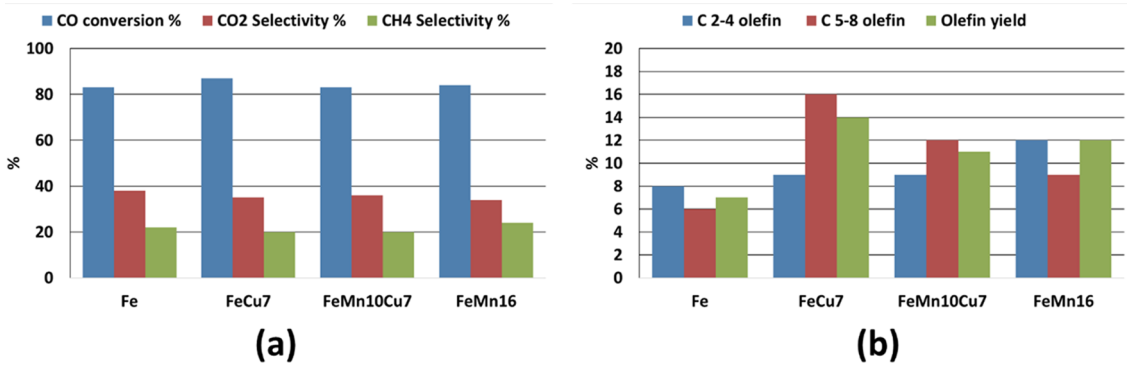

Figure 7. SBR performance plots showing (a) CO conversion, CO_2, and CH_4 selectivity, and (b) olefin selectivity of the C_{2-4} and C_{5-9} and total olefin yields for the Cu series compared with Fe and $FeMn_{16}$ at 340 °C, 2 MPa, and 4.2 L/(g h).

Table 4. Effect of Cu Promotion on the Fe Catalyst Performance at 300 °C in FBR[a]

	Fe	$FeCu_7$	$FeMn_{10}Cu_7$	$FeMn_{16}$
CO conversion (%)	14	76	87	46
carbon balance (%)	97	95	96	95
fraction	selectivity C (mol %)			
CO_2	64	63	53	45
CH_4	33	21	23	13
C2−4 olefin	12	29	30	27
C5−9 olefin	5	14	11	18
total olefin	17	43	43	49
C9 + HC	0.1	1	2	3
total paraffin	73	50	52	34
total iso	2	7	5	17
total par + iso	75	57	57	51
O/P	0.2	0.77	0.76	0.96
olefin yield	1	12	17	12
A	0.54	0.63	0.67	0.71

[a]Reaction conditions: H_2/CO = 1, 2 MPa, 300 °C, 4.2 L/(g h), TOS = 8 h.

Table 5. Effect of Cu Promotion on the Fe Catalyst Performance at 320 °C in FBR[a]

	Fe	$FeCu_7$	$FeMn_{10}Cu_7$	$FeMn_{16}$
CO conversion (%)	56	94	93	92
carbon balance (%)	95	96	97	97
fraction	selectivity C (mol %)			
CO_2	52	57	52	37
CH_4	39	22	28	8
C2−4 olefin	7	23	21	20
C5−9 olefin	3	18	13	25
total olefin	10	44	35	49
C9 + HC	0.3	2	2	21
total paraffin	87	52	59	26
total iso	4	4	6	25
total par + iso	91	56	65	51
O/P	0.1	0.79	0.55	0.96
olefin yield	3	18	22	29
A	0.51	0.61	0.59	0.77

[a]Reaction conditions: H_2/CO = 1, 2 MPa, 320 °C, 4.2 L/(g h).

8a,b that conversion and catalyst activity rises with temperature. In the case of Fe, there was a jump in conversion from 14% at 300 °C to 56% at 320 °C. The same observation was noticed with $FeMn_{16}$, which experienced a rise in conversion from 46% at 300 °C to 93% at 320 °C. For the other catalysts, the increase in conversion was not that intensive but still showed a positive change.

Most importantly, the Cu-promoted catalysts $FeCu_7$ and $FeMn_{10}Cu_7$ exhibited very high catalyst activity compared to other catalysts at 300 °C, with $FeCu_7$ causing a conversion of 76% and $FeMn_{10}Cu_7$ showing a conversion of 87%. This proves that Cu was successful in increasing the reducibility of the Fe catalysts, which increased the number of active catalyst sites and allowed for high catalyst activities even at T as low as 300 °C.[43,44,46,48] This is also evident from the TPR results, which showed an increase in H_2 consumption with the addition of Cu, and also from the BET area values, which increased by Cu promotion as well. It is also evident that there is a synergistic effect between Cu and Mn in $FeMn_{10}Cu_7$, which showed a maximum conversion of 87% at 300 °C.

Regarding the CO_2 selectivity, a look at Figures 8a,b and 9a shows the variation in CO_2 selectivity with temperature for each catalyst. We can deduce that, in general, the CO_2 selectivity falls steadily between Fe, $FeCu_7$, $FeMn_{10}Cu_7$, and $FeMn_{16}$, with $FeMn_{16}$ showing the lowest CO_2 selectivity at both temperatures. This observation contradicts the findings of other researchers[48] that indicate that Cu has a positive effect on the WGS reaction. However, O'Brien stated in his paper that the comparison of CO_2 selectivity was done at equal conversions, and in this case, the selectivities are a direct measure of the CO_2 yield, which is the product of CO_2 selectivity and conversion. Thus, if we want to compare the WGS activity of our catalysts, it would be more accurate to compare the CO_2 yields rather than the selectivities.

Figure 9b illustrates the values of CO_2 yield at 300 and 320 °C for the different catalysts. It is evident from Figure 9b that the yield for CO_2 increases by adding Cu and Mn to the Fe catalysts and that the effect of Cu is more pronounced than that of Mn. It is also clear that Mn mitigated the effect of Cu on the WGS activity in case of $FeMn_{10}Cu_7$, which showed a yield of 46 and 48%, respectively, as compared to the maximum values of 48 and 54% with $FeCu_7$ at 300 and 320 °C. The same can be said about the effect of temperature on the WGS activity, which showed a slight decrease in CO_2 selectivity from 320 to 300 °C with all catalysts, while showing an increase in CO_2 yield for all catalysts at the same temperatures.

Figure 8 also shows the methane selectivity for different catalysts at 300 and 320 °C. In general, the addition of Cu and Mn promoters to the catalyst decreased the CH_4 selectivity as compared with the unpromoted Fe catalyst, while temperature had a slight positive effect on the methane selectivity. It is well

https://doi.org/10.1021/acsomega.1c04476
ACS Omega 2021, 6, 31099−31111

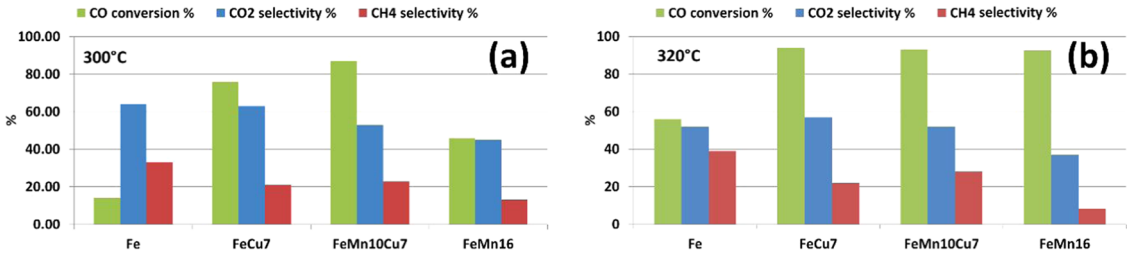

Figure 8. FBR performance plots showing CO conversion, and CO_2 and CH_4 selectivities for the Cu series compared with Fe and $FeMn_{16}$ at (a) 300 °C and (b) 320 °C.

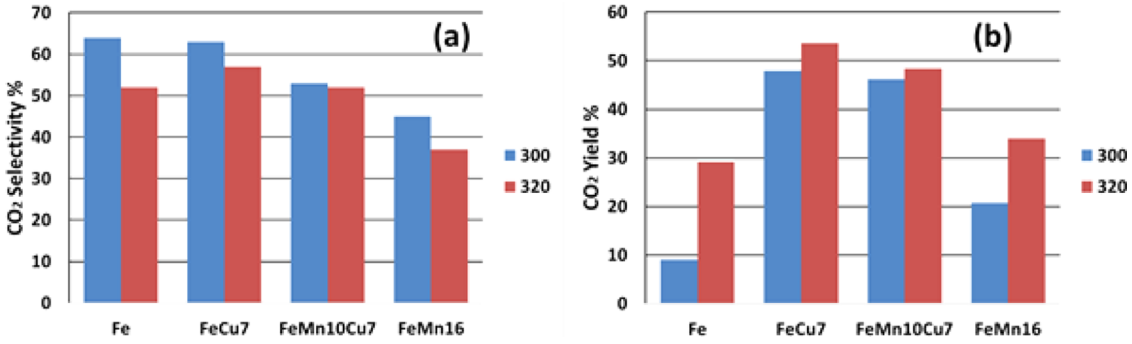

Figure 9. FBR performance plots showing (a) CO_2 selectivity and (b) CO_2 yield at 300 and 320 °C.

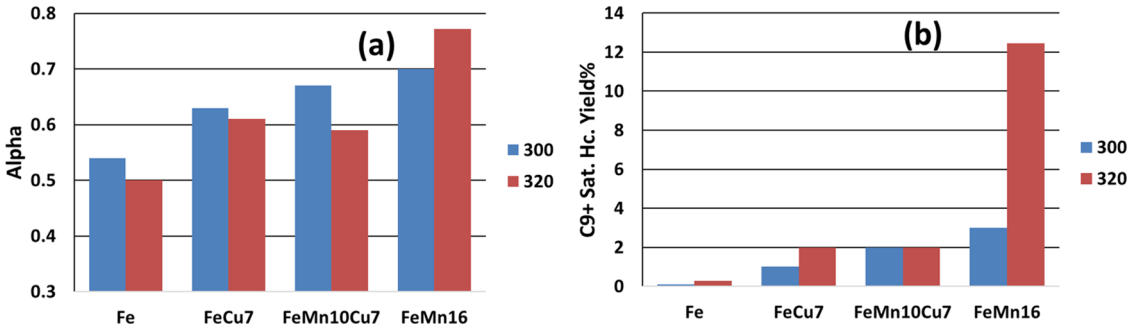

Figure 10. (a) ASF chain growth probability parameter and (b) C_9^+ Sat. HC. yield for the FBR performance of the catalysts at 300 and 320 °C.

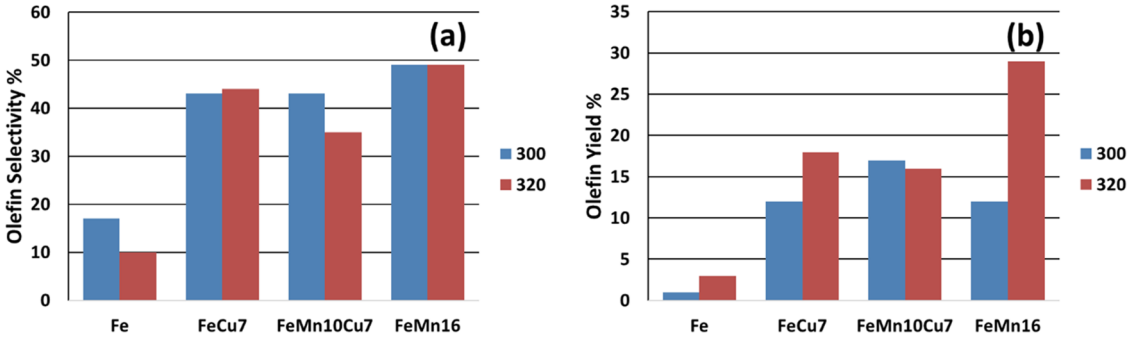

Figure 11. FBR performance plots showing (a) olefin selectivity and (b) olefin yield at 300 and 320 °C.

documented in previous research that Cu and Mn increase the average molecular weight of the hydrocarbon product[31,42,46,53] and reduce light selectivity, including methane, which is also evident from the increase in the α parameter and the C_9^+ saturated hydrocarbon yield displayed in Figure 10, which shows the variation of α and the C_9^+ saturated hydrocarbon yield with all catalysts at 300 and 320 °C.

Figure 11a,b shows the trend in olefin selectivity and yield for the different catalysts at 300 and 320 °C. it is obvious from both figures that adding Cu and Mn promoters had a strong positive effect on the olefinity of the product. In all promoted catalysts the selectivity jumped from a maximum of 17% with Fe at 300 °C to above 30%. The effect of Mn was more significant than that of copper, where the selectivity leveled at 49% for $FeMn_{16}$ at 300 and 320 °C. $FeCu_7$ recorded a selectivity of 43 and 44% at 300 and 320 °C, respectively, while $FeMn_{10}Cu_7$ produced olefins at a selectivity of 43 and 35% at 300 and 320 °C, respectively.

https://doi.org/10.1021/acsomega.1c04476
ACS Omega 2021, 6, 31099−31111

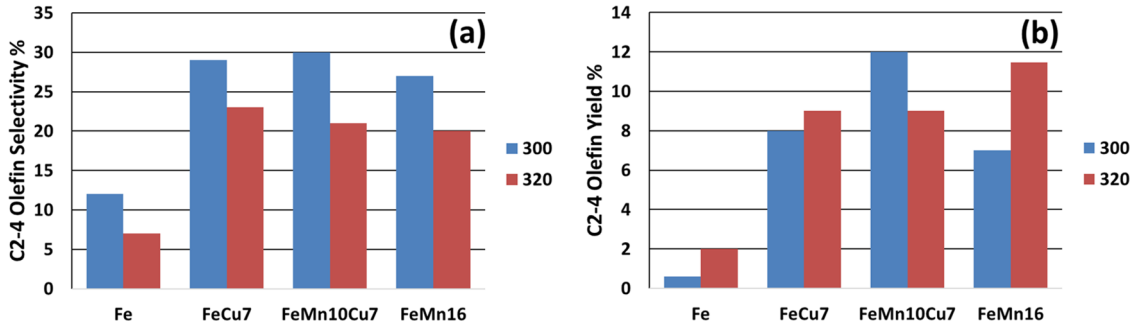

Figure 12. FBR performance plots showing the C2−4 olefin (a) selectivity and (b) yield at 300 and 320 °C.

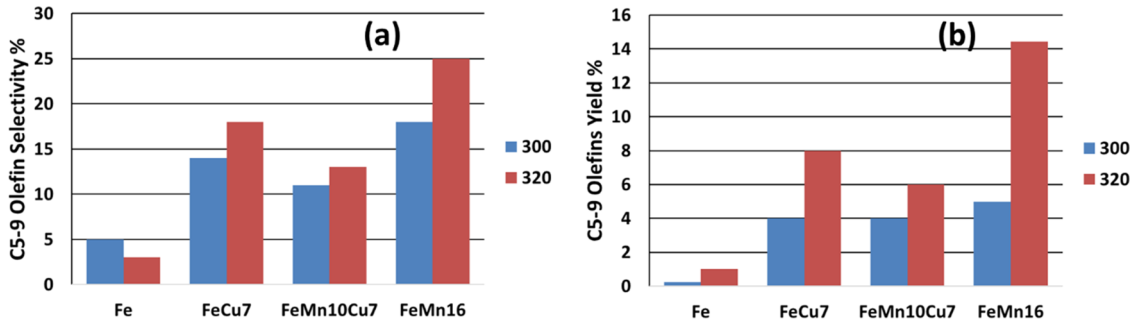

Figure 13. FBR performance plots showing the C5−9 olefin (a) selectivity and (b) yield at 300 and 320 °C.

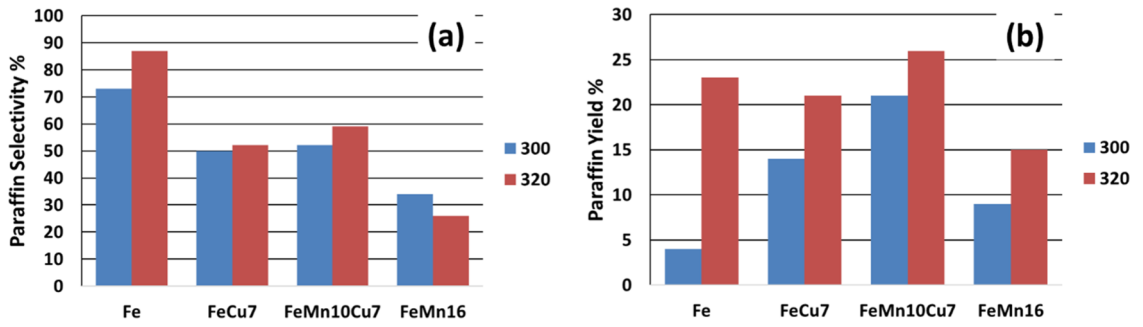

Figure 14. FBR performance plots showing the paraffin (a) selectivity and (b) yield at 300 and 320 °C.

The olefin yield showed a similar trend to selectivity, with Cu influencing a rise in olefin yield. However, the effect of $FeMn_{16}$ on olefin yield at 320 °C was not surpassed by any other catalyst, which produced olefins with a yield of 29%. It was mentioned in the introduction that the effect of Cu on the product selectivity and especially the olefinity of the product was not clear in the literature, and there was a contradiction between the opinions of previous researchers, where some claimed that Cu had no effect on product distribution, while others stated that it had a positive influence on olefin productivity. It is our opinion and based on the findings we present in this work that Cu does have a positive influence on the olefinity of the hydrocarbon product, which is evident from Figure 11a,b.

The effect of adding Cu and Mn as promoters to the Fe catalyst on the quality of the olefin fraction is demonstrated in Figures 12 and 13, which display the selectivities and yields of the C_{2-4} and the C_{5-9} olefin fractions for all catalysts at 300 and 320 °C, respectively. By looking at these plots, we can claim that Cu and Mn promotion increases the selectivity and yield of both olefin fractions. $FeMn_{10}Cu_7$ was more effective in enhancing the C_{2-4} olefin productivity, giving a maximum yield of 12% at 300 °C, while $FeMn_{16}$ gave the highest C_{5-9} olefin yield of 14% at 320 °C. The olefin fraction produced by the $FeCu_7$ and $FeMn_{10}Cu_7$ was richer in C_{2-4} olefins than in C_{5-9} olefins at all temperatures. This allows the proposed FT process to be tailored for different product qualities by changing the catalyst composition and operating conditions according to the demands of the market.

Figure 14a,b illustrates the paraffin selectivity and yield for all catalysts at 300 and 320 °C. it is evident from Figure 14a that Cu and Mn decreased the selectivity of Fe to paraffins. Fe showed a maximum selectivity of 73 and 87% at 300 and 320 °C, respectively. The addition of Cu in $FeCu_7$ and $FeMn_{10}Cu_7$ levelled the selectivity down to between 50 and 60%, while Mn was the most effective in suppressing the paraffin selectivity, keeping it at 34 and 26% at 300 and 320 °C, respectively.

On the other hand, the paraffin yield in Figure 14b showed an opposing behavior at 300 °C, where it appears that Cu and Mn promotion increased the paraffin yield, with $FeMn_{10}Cu_7$ having a synergistic effect on the paraffin yield, giving a maximum of 21%. This is clarified by looking at the effect of Cu and Mn on the CO conversion and the CO_2 selectivity discussed previously, which contributes mathematically to the calculation of the yield. The jump in CO conversion from 14% for Fe to 76 and 87% for

https://doi.org/10.1021/acsomega.1c04476
ACS Omega 2021, 6, 31099−31111

$FeCu_7$ and $FeMn_{10}Cu_7$, respectively, is the major cause for the rise in paraffin yield from 4% with Fe to 14 and 21% with $FeCu_7$ and $FeMn_{10}Cu_7$, respectively. The effect of the decrease in CO_2 selectivity also contributed, but not as significantly as the effect of conversion. Mn in $FeMn_{16}$, on the other hand, caused only a slight increase in paraffin selectivity (9%) due to its modest conversion of only 46%. At 320 °C, the image of the paraffin yield was different, with Fe, $FeCu_7$, and $FeMn_{10}Cu_7$ having a high yield for paraffins (20−25%), while $FeMn_{16}$ had the lowest paraffin yield of all catalysts (15%). This is due to its small paraffin selectivity (26%) and the high olefin selectivity (49%), which lowered the yield of the paraffins albeit the very high activity of $FeMn_{16}$ (92%) at 320 °C.

3.6. Comparison between the SBR and FBR Performance. In brief, we will discuss the reasons for the difference in performance between the SBR and FBR systems in the Cu-promoted FTS catalysis. It is evident from Figure 15 and Tables 3−5 that the catalyst activity and CO conversion in the SBR was lower than the FBR except with the Fe catalyst. The conversion in the SBR levelled at about 85% for all of the catalysts at 340 °C, while the FBR catalyst activity was well above 90% for the Cu- and Mn-promoted catalysts at only 320 °C. The effect of Cu as a Fe reduction promoter and its positive influence on the catalyst activity are not that significant in the SBR study since all the catalysts gave about the same conversion regardless of the presence of a promoter.

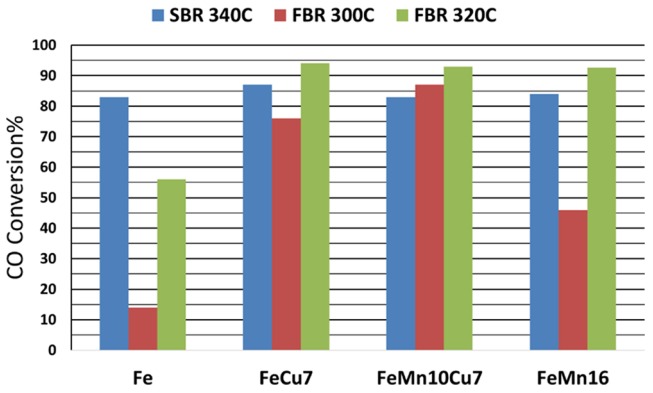

Figure 15. CO Conversion in the SBR at 340 °C and in the FBR at 300 and 320 °C.

In catalysis reactions, there could be one of two performance modes: diffusion-controlled performance and chemically controlled performance. It is evident from Figure 15 and Tables 3−5 that the SBR performance was the former mode, i.e., diffusion controlled. This is comprehensible, as the SBR adds a new barrier against the diffusion of reactants from the gas phase to the surface of the catalyst. In the SBR, reactants have to go through the gas bulk, the gas−liquid interface, the liquid bulk, and the liquid−solid interface, and then diffuse inside the catalyst pores to reach the active site to react. These barriers are much less in the FBR, where the reactants only diffuse through the gas bulk and the gas−solid interface and then diffuse inside the catalyst pores to reach the active sites.

The limiting step in the SBR is the diffusion through the liquid medium, and the amount of reactants reaching the catalyst surface are less than that expected based on the catalyst's ability to carry out the FTS reaction. This is why the upper limit of the conversion is not improved by the presence of promoters. If we wish to improve the conversion of the SBR system, we should try to change the reactor design to increase the mass transfer rate of the reactants from the gas to the catalyst surface by adding baffles or increasing the agitation speed of the impeller.

3.7. Comparison with Previous Work. The obtained results of our study were compared with other studies as depicted in Table 6. As can be seen, the table can be divided into 4 main groups: the Co-based catalysts, the bimetallic catalysts, the Fe-based catalysts, and this work as presented in the last three rows. In case of the cobalt-based catalyst, there was no data available about the olefin selectivity, and the catalysts were more suitable for producing linear alkanes and diesel fractions at high selectivities >90%. With the bimetallic catalysts, the olefin productivity was more pronounced than with cobalt alone, which would be expected when Fe is introduced in the catalyst structure. However, there is a mismatch between the conversion and selectivity in both cases mentioned in the table, so that when one of them is high the other would be low, which would in general decrease the olefin yield. Considering the Fe-based catalysts, they were most promising in producing olefins at high productivity, especially Fe-$MnCu_3/SiO_2$. This system is interesting in many ways: Firstly, it utilized the FBR, while the other two Fe-based systems utilized SBRs, and the FBR system

Table 6. Comparison between the Current Study and Previous Reported Studies

				selectivity fraction C (mol %)				
FTS catalyst	FTS conditions	FTS reactor	CO conversion (%)	CO_2	CH_4	total olefin	total (par + iso)	ref
25Co, 0.5Ru/N-GNS	220 °C, 1.8 MPa, H_2/CO = 2, 5.2 L/(g h)	FBR	86.9	0.80	7.7	n/a	91.2	54
45Fe 45Co 10Mn	290 °C, H_2/CO 1:1, GHSV 3000 h^{-1}, 2 bar	FBR	31.01	32.30	43.72	22.22	n/a	55
Co/Al_2O_4−0.08	235 °C, 2MPa, H_2/CO = 2, GHSV = 1000 h^{-1}	FBR	57.66	n/a	9.33	n/a	90.66	56
$10Fe/20Co/SiO_2$	240 C, Syn-biomass, 2 MPa, SV-2000 mL/(g_{cat}.h)	FBR	89.20	11.43	26.00	7.50	79.00	57
100Fe/4.6Si/1.4K	H_2/ CO = 0.67, 1.3 MPa, 270 °C, 65 L/(g h)	STR	20	30	5.5	41.2	58.8	16
100Fe:5.1Si:1.25K:5.0Cu	T = 270 °C, 175 psi, H_2/CO = 0.7, 3 sL/g_{cat}.h	CSTR	81.5	46.3	4.1	n/a	95.9	58
Fe-$MnCu_3/SiO_2$	300 °C, 20 bar, GHSV = 1500 h^{-1}, H_2/CO = 2	FBR	96.9	23	20	40.1	66.1	59
Fe−$Mn_{10}Cu_7$/rGO	H_2/CO = 1, 2 MPa, 340 °C, 4.2 L/(g h)	SBR	83	36	20	21	79	this work
Fe−$Mn_{10}Cu_7$/rGO	H_2/CO = 1, 2 MPa, 300 °C, 4.2 L/(g h)	FBR	87	46	23	49	51	this work
Fe−$Mn_{10}Cu_7$/rGO	H_2/CO = 1, 2 MPa, 320 °C, 4.2 L/(g h)	FBR	93	48	28	49	51	this work

https://doi.org/10.1021/acsomega.1c04476
ACS Omega 2021, 6, 31099−31111

gave the best olefin selectivity, as we suggested in this work. Secondly, the catalyst has a very similar composition to the ternary catalyst used in this study, except that their support is silica, whereas ours is graphene. However, it can be seen from the table that the performance of this system is very much comparable to the $FeMn_{10}Cu_7$ in the FBR at 300 and 320 °C, which further reinforces the results of our study.

4. CONCLUSIONS

In conclusion, Cu acted as a reduction promoter speeding up the reduction of hematite into metallic Fe, and the effect of Cu as a promoter was stronger in FBR test runs than SBR test runs due to mass transfer (diffusion-controlled) limitations in the SBR. In the SBR experiments, the catalyst activity at 340 °C was less than that in the FBR at only 320 °C, except for the Fe catalyst. This reduced activity was attributed to the diffusion-controlled reaction due to the resistance of the liquid in the slurry to the diffusion of the reactants to the catalyst surface. Also, Cu alone increased the olefinity, but when used with Mn, it only shifted the selectivity slightly towards heavier olefins while keeping the total olefin selectivity constant.

We can deduce the following about the effect of Cu promotion on the FTS performance of Fe catalysts in the FBR at HTFT conditions:

- Cu promotion increases catalyst activity significantly.
- CO_2 yield increases due to the high FT activity even though CO_2 selectivity is slightly decreased by Cu promotion.
- Olefinity is positively affected by Cu promotion, even if the olefin yield of $FeMn_{16}$ at 320 °C is not yet surpassed.
- The paraffinity of the product is enhanced by Cu promotion and there is a synergistic effect between Cu and Mn in this respect.
- Cu is more effective in enhancing paraffin yield than olefin yield, as opposed to Mn, which enhances olefinity more effectively.
- Cu promotion produces an olefin fraction richer in the light olefins C2−4.

AUTHOR INFORMATION

Corresponding Authors

Al-Hassan Nasser − *Chemical Engineering Department, Faculty of Engineering, Alexandria University, Alexandria 11432, Egypt*; Email: Alhassan.Nasser@alexu.edu.eg

Haitham M. El-Bery − *Advanced Multifunctional Materials Laboratory, Chemistry Department, Faculty of Science, Assiut University, Assiut 71515, Egypt*; orcid.org/0000-0003-2234-0455; Email: Haitham.El-Bery@aun.edu.eg

Authors

Hamada ELnaggar − *Materials Science and Engineering Department, Egypt-Japan University of Science and Technology, New Borg El-Arab, Alexandria 21934, Egypt*

Islam K. Basha − *Materials Science and Engineering Department, Egypt-Japan University of Science and Technology, New Borg El-Arab, Alexandria 21934, Egypt; Chemistry Department, Faculty of Science, Alexandria University, Alexandria 11432, Egypt*

Ahmed Abd El-Moneim − *Materials Science and Engineering Department, Egypt-Japan University of Science and Technology, New Borg El-Arab, Alexandria 21934, Egypt; Nanoscience Program, Institute of Basic and Applied Sciences, Egypt-Japan University of Science and Technology, New Borg El Arab City, Alexandria 21934, Egypt*

Complete contact information is available at: https://pubs.acs.org/10.1021/acsomega.1c04476

Notes

The authors declare no competing financial interest.

ACKNOWLEDGMENTS

This research was conducted as a part of the Research Project (ID 4543, 7825) supported by the Science and Technology Development Fund (STDF) and Academy of Scientific Research and Technology in Egypt. The authors would like to acknowledge Prof. Noritatsu Tsubaki for allowing them to carry out the SBR experiments in his lab.

REFERENCES

(1) Hou, Y.; Li, J.; Qing, M.; Liu, C.-L.; Dong, W.-S. Direct synthesis of lower olefins from syngas via Fischer−Tropsch synthesis catalyzed by a dual-bed catalyst. *Mol. Catal.* **2020**, *485*, No. 110824.

(2) Ma, Z.; Ma, H.; Zhang, H.; Wu, X.; Qian, W.; Sun, Q.; Ying, W. Direct Conversion of Syngas to Light Olefins through Fischer-Tropsch Synthesis over Fe-Zr Catalysts Modified with Sodium. *ACS Omega* **2021**, *6*, 4968−4976.

(3) Boulamanti, A.; Moya, J. A. Production costs of the chemical industry in the EU and other countries: Ammonia, methanol and light olefins. *Renewable Sustainable Energy Rev.* **2017**, *68*, 1205−1212.

(4) Amghizar, I.; Vandewalle, L. A.; Van Geem, K. M.; Marin, G. B. New Trends in Olefin Production. *Engineering* **2017**, *3*, 171−178.

(5) Zhang, Q.; Hu, S.; Chen, D. A comparison between coal-to-olefins and oil-based ethylene in China: An economic and environmental prospective. *J. Cleaner Prod.* **2017**, *165*, 1351−1360.

(6) Tomasek, S.; Lonyi, F.; Valyon, J.; Wollmann, A.; Hancsok, J. Hydrocracking of Fischer-Tropsch Paraffin Mixtures over Strong Acid Bifunctional Catalysts to Engine Fuels. *ACS Omega* **2020**, *5*, 26413−26420.

(7) Liu, J.; Tian, F.; Liu, J.; Guo, Q.; Fan, X.; Dan, Y.; Fu, Q.; Du, Z.; Han, W.; Song, D.; Li, D. Structure Characterization and Solubility Analysis of the Existent Gum of the Fischer-Tropsch Synthetic Crude. *ACS Omega* **2020**, *5*, 18778−18786.

(8) Govender, A.; Olivier, E. J.; Haigh, S. J.; Kelly, D.; Smith, M.; van Rensburg, H.; Forbes, R. P.; van Steen, E. Performance of a NiFe2O4@Co Core-Shell Fischer-Tropsch Catalyst: Effect of Low Temperature Reduction. *ACS Omega* **2020**, *5*, 32975−32983.

(9) Yang, S.; Li, M.; Nawaz, M. A.; Song, G.; Xiao, W.; Wang, Z.; Liu, D. High Selectivity to Aromatics by a Mg and Na Co-modified Catalyst in Direct Conversion of Syngas. *ACS Omega* **2020**, *5*, 11701−11709.

(10) Santos, R. G. d.; Alencar, A. C. Biomass-derived syngas production via gasification process and its catalytic conversion into fuels by Fischer Tropsch synthesis: A review. *Int. J. Hydrogen Energy* **2020**, *45*, 18114−18132.

(11) Tawfik, A.; El-Bery, H.; Elsamadony, M.; Kumari, S.; Bux, F. Upgrading continuous H2 gas recovery from rice straw hydrolysate via fermentation process amended with magnetite nanoparticles. *Int. J. Energy Res.* **2019**, *43*, 3516−3527.

(12) Mahmoud, A. H.; El-Bery, H. M.; Ali, M. M.; Aldaby, E. S.; Mawad, A. M. M.; Shoreit, A. A. Latex-bearing plant (Calotropis procera) as a biorefinery for bioethanol production *Biomass Convers. Biorefin.* 2021, DOI: 10.1007/s13399-021-01479-w.

(13) El-Bery, H. M.; Salah, M. R.; Ahmed, S. M.; Soliman, S. A. Efficient non-metal based conducting polymers for photocatalytic hydrogen production: comparative study between polyaniline, polypyrrole and PEDOT. *RSC Adv.* **2021**, *11*, 13229−13244.

(14) El-Bery, H. M.; Abdelhamid, H. N. Photocatalytic hydrogen generation via water splitting using ZIF-67 derived Co3O4@C/TiO2. *J. Environ. Chem. Eng.* **2021**, *9*, No. 105702.

(15) Li, J.; Hou, Y.; Song, Z.; Liu, C.; Dong, W.; Zhang, C.; Yang, Y.; Li, Y. Chemical and structural effects of strontium on iron-based Fischer-Tropsch synthesis catalysts. *Mol. Catal.* **2018**, *449*, 1−7.
(16) Abbas, M.; Zhang, J.; Mansour, T. S.; Chen, J. Hierarchical porous spinel MFe2O4 (M=Fe, Zn, Ni and Co) nanoparticles: Facile synthesis approach and their superb stability and catalytic performance in Fischer-Tropsch synthesis. *Int. J. Hydrogen Energy* **2020**, *45*, 10754−10763.
(17) Zhang, Y.; Hanayama, K.; Tsubaki, N. The surface modification effects of silica support by organic solvents for Fischer−Tropsch synthesis catalysts. *Catal. Commun.* **2006**, *7*, 251−254.
(18) Bao, J.; Yang, G.; Okada, C.; Yoneyama, Y.; Tsubaki, N. H-type zeolite coated iron-based multiple-functional catalyst for direct synthesis of middle isoparaffins from syngas. *Appl. Catal., A* **2011**, *394*, 195−200.
(19) Torres Galvis, H. M.; Koeken, A. C. J.; Bitter, J. H.; Davidian, T.; Ruitenbeek, M.; Dugulan, A. I.; de Jong, K. P. Effects of sodium and sulfur on catalytic performance of supported iron catalysts for the Fischer−Tropsch synthesis of lower olefins. *J. Catal.* **2013**, *303*, 22−30.
(20) Abrokwah, R. Y.; Rahman, M. M.; Deshmane, V. G.; Kuila, D. Effect of titania support on Fischer-Tropsch synthesis using cobalt, iron, and ruthenium catalysts in silicon-microchannel microreactor. *Mol. Catal.* **2019**, *478*, No. 110566.
(21) Mosallanejad, S.; Dlugogorski, B. Z.; Kennedy, E. M.; Stockenhuber, M. On the Chemistry of Iron Oxide Supported on gamma-Alumina and Silica Catalysts. *ACS Omega* **2018**, *3*, 5362−5374.
(22) Hamad, H. A.; Nageh, H.; El-Bery, H. M.; Kasry, A.; Carrasco-Marin, F.; Elhady, O. M.; Soliman, A. M. M.; El-Remaily, M. Unveiling the exceptional synergism-induced design of Co-Mg-Al layered triple hydroxides (LTHs) for boosting catalytic activity toward the green synthesis of indol-3-yl derivatives under mild conditions. *J. Colloid Interface Sci.* **2021**, *599*, 227−244.
(23) Yang, Z.; Pan, X.; Wang, J.; Bao, X. FeN particles confined inside CNT for light olefin synthesis from syngas: Effects of Mn and K additives. *Catal. Today* **2012**, *186*, 121−127.
(24) Xu, J.-D.; Zhu, K.-T.; Weng, X.-F.; Weng, W.-Z.; Huang, C.-J.; Wan, H.-L. Carbon nanotube-supported Fe−Mn nanoparticles: A model catalyst for direct conversion of syngas to lower olefins. *Catal. Today* **2013**, *215*, 86−94.
(25) van Deelen, T. W.; Yoshida, H.; Oord, R.; Zečević, J.; Weckhuysen, B. M.; de Jong, K. P. Cobalt nanocrystals on carbon nanotubes in the Fischer-Tropsch synthesis: Impact of support oxidation. *Appl. Catal., A* **2020**, *593*, No. 117441.
(26) Cheng, Y.; Lin, J.; Xu, K.; Wang, H.; Yao, X.; Pei, Y.; Yan, S.; Qiao, M.; Zong, B. Fischer−Tropsch Synthesis to Lower Olefins over Potassium-Promoted Reduced Graphene Oxide Supported Iron Catalysts. *ACS Catal.* **2016**, *6*, 389−399.
(27) Hajjar, Z.; Doroudian Rad, M.; Soltanali, S. Novel Co/graphene oxide and Co/nanoporous graphene catalysts for Fischer−Tropsch reaction. *Res. Chem. Intermed.* **2017**, *43*, 1341−1353.
(28) Huang, J.; Qian, W.; Ma, H.; Zhang, H.; Ying, W. Highly selective production of heavy hydrocarbons over cobalt−graphene−silica nanocomposite catalysts. *RSC Adv.* **2017**, *7*, 33441−33449.
(29) Nasser, A. H. M.; Elbery, H. M.; Anwar, H. N.; Basha, I. K.; Elnaggar, H. A.; Nakamura, K.; El-Moneim, A. A. A Study of Promoters Effect on Fe on Reduced Graphene Oxide Catalyst Performance in Fischer-Tropsch Synthesis System. *Key Eng. Mater.* **2017**, *735*, 143−147.
(30) Taghavi, S.; Asghari, A.; Tavasoli, A. Enhancement of performance and stability of Graphene nano sheets supported cobalt catalyst in Fischer−Tropsch synthesis using Graphene functionalization. *Chem. Eng. Res. Des.* **2017**, *119*, 198−208.
(31) Nasser, A. L. H.; El-Naggar, H.; El-Bery, H.; Basha, I.; Abdelmoneim, A. Correction: Utilizing FBR to produce olefins from CO reduction using Fe−Mn nanoparticles on reduced graphene oxide catalysts and comparing the performance with SBR. *RSC Adv.* **2019**, *9*, 10937.
(32) Elnaggar, H. A.; Nasser, A. L. H. M.; Basha, I. K.; Elbery, H. M.; Abd El-Moneim, A. Study of the Reduction of Fe on Reduced Graphene Oxide as a Catalyst for Carbon Monoxide Reduction. *Key Eng. Mater.* **2020**, *835*, 130−134.
(33) Nabil, S.; Hammad, A. S.; El-Bery, H. M.; Shalaby, E. A.; El-Shazly, A. H. The CO2 photoconversion over reduced graphene oxide based on Ag/TiO2 photocatalyst in an advanced meso-scale continuous-flow photochemical reactor. *Environ. Sci. Pollut. Res.* **2021**, *28*, 36157−36173.
(34) Santos, V. P.; Wezendonk, T. A.; Jaen, J. J.; Dugulan, A. I.; Nasalevich, M. A.; Islam, H. U.; Chojecki, A.; Sartipi, S.; Sun, X.; Hakeem, A. A.; Koeken, A. C.; Ruitenbeek, M.; Davidian, T.; Meima, G. R.; Sankar, G.; Kapteijn, F.; Makkee, M.; Gascon, J. Metal organic framework-mediated synthesis of highly active and stable Fischer-Tropsch catalysts. *Nat. Commun.* **2015**, *6*, No. 6451.
(35) Cruz, M. G. A.; Bastos-Neto, M.; Oliveira, A. C.; Filho, J. M.; Soares, J. M.; Rodríguez-Castellón, E.; Fernandes, F. A. N. On the structural, textural and morphological features of Fe-based catalysts supported on polystyrene mesoporous carbon for Fischer−Tropsch synthesis. *Appl. Catal., A* **2015**, *495*, 72−83.
(36) Bai, L.; Xiang, H.; Li, y.-w.; Han, Y.-Z.; Zhong, B. Slurry phase Fischer-Tropsch synthesis over manganese-promoted iron ultrafine particle catalyst. *Fuel* **2002**, *81*, 1577−1581.
(37) Cheng, Y.; Lin, J.; Wu, T.; Wang, H.; Xie, S.; Pei, Y.; Yan, S.; Qiao, M.; Zong, B. Mg and K dual-decorated Fe-on-reduced graphene oxide for selective catalyzing CO hydrogenation to light olefins with mitigated CO2 emission and enhanced activity. *Appl. Catal., B* **2017**, *204*, 475−485.
(38) de la Peña O'Shea, V. A.; Alvarez-Galvan, M. C.; Campos-Martin, J. M.; Fierro, J. L. G. Strong dependence on pressure of the performance of a Co/SiO2 catalyst in Fischer−Tropsch slurry reactor synthesis. *Catal. Lett.* **2005**, *100*, 105−116.
(39) Zhang, C.-H.; Wan, H.-J.; Yang, Y.; Xiang, H.-W.; Li, Y.-W. Study on the iron−silica interaction of a co-precipitated Fe/SiO2 Fischer−Tropsch synthesis catalyst. *Catal. Commun.* **2006**, *7*, 733−738.
(40) Luque, R.; de la Osa, A. R.; Campelo, J. M.; Romero, A. A.; Valverde, J. L.; Sanchez, P. Design and development of catalysts for Biomass-To-Liquid-Fischer−Tropsch (BTL-FT) processes for biofuels production. *Energy Environ. Sci.* **2012**, *5*, 5186−5202.
(41) BARTHOLOMEW, C. H. RECENT TECHNOLOGICAL DEVELOPMENTS IN FISCHER-TROPSCH CATALYSIS. *Catal. Lett.* **1991**, *7*, 303−316.
(42) Zhang, C.; Yang, Y.; Teng, B.; Li, T.; Zheng, H.; Xiang, H.; Li, Y. Study of an iron-manganese Fischer−Tropsch synthesis catalyst promoted with copper. *J. Catal.* **2006**, *237*, 405−415.
(43) Wan, H.; Wu, B.; Zhang, C.; Xiang, H.; Li, Y. Promotional effects of Cu and K on precipitated iron-based catalysts for Fischer−Tropsch synthesis. *J. Mol. Catal. A: Chem.* **2008**, *283*, 33−42.
(44) de Smit, E.; de Groot, F. M.; Blume, R.; Havecker, M.; Knop-Gericke, A.; Weckhuysen, B. M. The role of Cu on the reduction behavior and surface properties of Fe-based Fischer-Tropsch catalysts. *Phys. Chem. Chem. Phys.* **2010**, *12*, 667−680.
(45) Zhao, X.-h.; Li, Y.-w.; Wang, J.-g.; Huo, C.-f. CO adsorption, CO dissociation, and C-C coupling on Cu monolayer-covered Fe(100). *J. Fuel Chem. Technol.* **2011**, *39*, 956−960.
(46) Bukur, D. B.; Doble, Mukesh.; Pate1, S. A. Promoter Effects on Precipitated Iron Catalysts for Fischer-Tropsch Synthesis. *Ind. Eng. Chem. Res.* **1990**, *29*, 194−204.
(47) Özkara-Aydınoğlu, Ş.; Ataç, Ö.; Gül, ÖF.; Kınayyiğit, Ş.; Şal, S.; Baranak, M.; Boz, İ. α-olefin selectivity of Fe−Cu−K catalysts in Fischer−Tropsch synthesis: Effects of catalyst composition and process conditions. *Chem. Eng. J.* **2012**, *181−182*, 581−589.
(48) O'Brien, R. J.; Davis, B. H. Impact of copper on an alkali promoted iron Fischer−Tropsch catalyst. *Catal. Lett.* **2004**, *94*, 1−6.
(49) El-Bery, H. M.; Matsushita, Y.; Abdel-moneim, A. Fabrication of efficient TiO2-RGO heterojunction composites for hydrogen generation via water-splitting: Comparison between RGO, Au and Pt reduction sites. *Appl. Surf. Sci.* **2017**, *423*, 185−196.
(50) Gamil, M.; Tabata, O.; Nakamura, K.; El-Bab, A. M. R. F.; El-Moneim, A. A. Investigation of a New High Sensitive Micro-

https://doi.org/10.1021/acsomega.1c04476
ACS Omega 2021, 6, 31099−31111

Electromechanical Strain Gauge Sensor Based on Graphene Piezoresistivity. *Key Eng. Mater.* **2014**, *605*, 207−210.
(51) Rashed, A. E.; El-Moneim, A. A. Two steps synthesis approach of MnO2/graphene nanoplates/graphite composite electrode for supercapacitor application. *Mater. Today Energy* **2017**, *3*, 24−31.
(52) Moussa, S. O.; Panchakarla, L. S.; Ho, M. Q.; El-Shall, M. S. Graphene-Supported, Iron-Based Nanoparticles for Catalytic Production of Liquid Hydrocarbons from Synthesis Gas: The Role of the Graphene Support in Comparison with Carbon Nanotubes. *ACS Catal.* **2014**, *4*, 535−545.
(53) Nasser, A. L. H.; Guo, L.; Elnaggar, H.; Wang, Y.; Guo, X.; AbdelMoneim, A.; Tsubaki, N. Mn−Fe nanoparticles on a reduced graphene oxide catalyst for enhanced olefin production from syngas in a slurry reactor. *RSC Adv.* **2018**, *8*, 14854−14863.
(54) Taghavi, S.; Tavasoli, A.; Asghari, A.; Signoretto, M. Loading and promoter effects on the performance of nitrogen functionalized graphene nanosheets supported cobalt Fischer-Tropsch synthesis catalysts. *Int. J. Hydrogen Energy* **2019**, *44*, 10604−10615.
(55) Golestan, S.; Mirzaei, A. A.; Atashi, H. Fischer−Tropsch synthesis over an iron−cobalt−manganese (ternary) nanocatalyst prepared by hydrothermal procedure: Effects of nanocatalyst composition and operational conditions. *Int. J. Hydrogen Energy* **2017**, *42*, 9816−9830.
(56) Ding, J.; Zhao, W.; Zi, L.; Xu, X.; Liu, Q.; Zhong, Q.; Xu, Y. Promotional Effect of ZrO2 on supported FeCoK Catalysts for Ethylene Synthesis from catalytic CO2 hydrogenation. *Int. J. Hydrogen Energy* **2020**, *45*, 15254−15262.
(57) Sonal; Ahmad, E.; Upadhyayula, S.; Pant, K. K. Biomass-derived CO2 rich syngas conversion to higher hydrocarbon via Fischer-Tropsch process over Fe−Co bimetallic catalyst. *Int. J. Hydrogen Energy* **2019**, *44*, 27741−27748.
(58) Pendyala, V. R. R.; Jacobs, G.; Gnanamani, M. K.; Hu, Y.; MacLennan, A.; Davis, B. H. Selectivity control of Cu promoted iron-based Fischer-Tropsch catalyst by tuning the oxidation state of Cu to mimic K. *Appl. Catal., A* **2015**, *495*, 45−53.
(59) Gong, W.; Ye, R.-P.; Ding, J.; Wang, T.; Shi, X.; Russell, C. K.; Tang, J.; Eddings, E. G.; Zhang, Y.; Fan, M. Effect of copper on highly effective Fe-Mn based catalysts during production of light olefins via Fischer-Tropsch process with low CO2 emission. *Appl. Catal., B* **2020**, *278*, No. 119302.

https://doi.org/10.1021/acsomega.1c04476
ACS Omega 2021, 6, 31099−31111